RSC Advances

PAPER

View Article Online
View Journal | View Issue

Cite this: *RSC Adv.*, 2023, **13**, 34427

The enhanced properties and bioactivity of poly-ε-caprolactone/poly lactic-*co*-glycolic acid doped with carbonate hydroxyapatite–egg white

Diana Julaidy Patty, [ab] Ari Dwi Nugraheni,[a] Ika Dewi Ana, [cd] Aminatun, [e] Yessie Widya Sari,[f] Gunawarman[g] and Yusril Yusuf *[ad]

Received 2nd November 2023
Accepted 7th November 2023

DOI: 10.1039/d3ra07486b

rsc.li/rsc-advances

Synthetic polymers, such as PCL and PLGA, are among the main material choices in tissue engineering because of their stable structures and strong mechanical properties. In this study, we designed polycaprolactone (PCL)/polylactic-*co*-glycolate acid (PLGA) nanofibers doped with carbonate hydroxyapatite (CHA) and egg white (EW) with enhanced properties. The addition of CHA and EW significantly influenced the properties and morphology of PCL/PLGA nanofibers; whereby the CHA substitution (PCL/PLGA/CHA) greatly increased the mechanical properties related to the Young's modulus and EW doping (PCL/PLGA/CHA/EW) increased the elongation at break. Bioactivity tests of PCL/PLGA/CHA/EW after immersion in the SBF for 3 to 9 days showed increased fiber diameters and a good swelling capacity that could improve cell adhesion, while biocompatibility tests with NIH-3T3 fibroblast cells showed good cell proliferation (85%) after 48 h and antibacterial properties against *S. aureus*.

1. Introduction

Polycaprolactone (PCL) polymers are flexible materials, and the electrospun nets of polylactic-*co*-glycolate acid (PLGA)/PCL have shown strong mechanical properties. Adding PLGA as a doping agent in the PCL/PLGA electrospun net increases the potential of the composite, which plays an important role in many biomaterials and tissue engineering applications considering the improved biocompatibility, cell attachment, and cell proliferation.[7] Specifically, PCL/PLGA composite electrospun nanofibrous scaffolds have been extensively developed in tissue engineering[1] for neural regeneration,[2] guided bone regeneration,[3,4] and controlled drug release.[5,6]

Implant designs based on polymer and protein interactions play an important role in biomedical applications, especially wound healing, because such interactions can increase protein adsorption on the polymer surface. Chicken egg white (EW) as a natural polymer, contains complete nutrition (80% protein, 85–89% water, and cell culture media), supports cell viability, and biocompatibility, and increases *in vitro* bioactivity.[8] Lysozymes in EW have antibacterial properties and can hydrolyze specific polysaccharides that make up the cell walls of some Gram-positive bacteria.[9–12] Owing to their biodegradability, natural and synthetic polymers play essential roles in drug delivery, wound care, scaffold, dental, and cardiovascular applications.[13]

Advanced materials design in bone tissue engineering requires a combination of different materials to obtain superior properties (physiochemical, mechanical, and biological properties). Carbonate hydroxyapatite (CHA) is a synthetic bone graft substitute with a chemical composition identical to the bone mineral component. The hydroxyapatite (HA) present in the human body is not pure ($Ca_{10}(PO_4)_6(OH)_2$) but rather contains carbonate ions, which are essential for the breakdown of HAp in solution and play an important role in several biological processes, such as dental caries and bone resorption.

CHA is synthesized from biogenic materials containing large amounts of calcium carbonate by combining calcium and phosphate sources, such as mammalian bones, shells,[11,14,15] coral, and egg shells. One biogenic material particularly high in calcium carbonate is pearl shell (*Pinctada maxima*), which, also because of being abundant, has significant potential for use in the synthesis of CHA for bone tissue reconstruction.[16] The carbonate group can replace hydroxyl ions (type-A carbonate/CHA type-A) and phosphate (type-B carbonate/CHA type B) in the hydroxyapatite structure. CHA type-B in the apatite lattice

[a]*Department of Physics, Faculty of Mathematics and Natural Science, Universitas Gadjah Mada, Yogyakarta, Indonesia*

[b]*Department of Physics, Faculty of Mathematics and Natural Science, Universitas Pattimura, Ambon, Indonesia*

[c]*Department of Dental Biomedical Sciences, Faculty of Dentistry, Universitas Gadjah Mada, Yogyakarta, Indonesia*

[d]*Research Collaboration Center for Biomedical Scaffolds National Research and Innovation Agency of the Republic of Indonesia (BRIN), Universitas Gadjah Mada (UGM), Bulaksumur, Yogyakarta 55281, Indonesia*

[e]*Department of Physics, Universitas Airlangga, Surabaya 60115, Indonesia*

[f]*Department of Physics, Institut Pertanian Bogor, Bogor 16680, Indonesia. E-mail: yusril@ugm.ac.id*

[g]*Department of Mechanical Engineering, Universitas Andalas, Padang 25163, Indonesia*

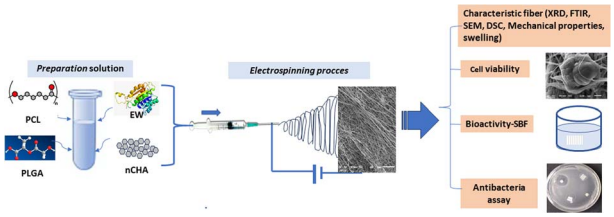

Fig. 1 A schematic showing the electrospinning process and nanofiber characterization.

has been shown to cause a decrease in crystallinity and increase solubility in *in vitro* and *in vivo* tests.[17]

One of the most demanding medical applications is the repair and formation of musculoskeletal tissue, especially bone, where a scaffold is needed that must have a high elastic modulus to provide temporary mechanical support without showing symptoms of fatigue or failure to maintain the repair in place while providing tissues with adequate space for growth.[18] Furthermore, it has antibacterial properties to prevent bacterial invasion, which can help prevent failure during application. Implant-based nanofibers could provide many advantages when designed with uniform and continuous nanofibers, including a porous structure with highly interconnected porosity, and a good swelling capacity, thus increasing the ability for cell adhesion.

This study aimed to design and analyze the polymer–bioceramic–protein interactions of PCL/PLGA doped with CHA-EW as a multifunctional bone graft (Fig. 1) by analyzing the physicochemical, mechanical properties, bioactivity, biocompatibility (NIH-3T3 fibroblast cells), and antibacterial activity of the doped material.

2. Materials and methods

2.1 Materials

PCL (Mn = 80 000, viscosity 2.2 dL g^{-1}), and PLGA (lactide : glycolide (75 : 25), mol wt 66 000–107 000) were purchased from Sigma Aldrich. *N*,*N*-Dimethylformamide (DMF) was purchased from Sigma Aldrich. CaO, diammonium hydrogen phosphate ($[NH_4]_2HPO_4$), ammonium hydroxide (NH_4OH) were obtained as a 25% solution from Merck (Kenilworth, NJ, USA). Ammonium bicarbonate (NH_4HCO_3) was purchased from PT Brataco (Indonesia). CHA was synthesized from the P. maxima shell. EW powder was obtained from Distributor Co Id Teknoboga (Central Jakarta, Indonesia). Fibroblast cells (NIH-3T3), DMEM high glucose medium (Gibco, CA, USA), 10% bovine calf serum supplementation were obtained from Sigma (MA, USA). Pen Strep 2% and Fungizone 0.5% were obtained from Gibco (CA, USA).

2.2 Synthesis of carbonate hydroxyapatite

The CHA synthesis followed the protocol reported in a previous study[12] by extracting CaO as a source of calcium from *P. maxima* shells. After the synthesis and aging for 24 h, the obtained CHA slurry was filtered using Whatman 42 filter paper. The CHA was dried in an oven for 6 h, without annealing, and then the physicochemical properties were characterized by SEM, XRD, and FTIR.

2.3 Electrospinning process

Electrospun nanofiber membranes were designed using the Electrospinning Nanosense-UGM device in the Materials and Instrumentation Physics Laboratory, Department of Physics, Faculty of Mathematics and Natural Sciences, UGM.

The PCL 10% w/v and PLGA 10% w/v spinning solutions were prepared using DMF and stirred with a magnetic stirrer at 40 °C for 6 h (700 rpm) until the solution was homogeneous. CHA powder was added to the PCL/PLGA solution and stirred until homogeneous for ~24 h. Then, homogenized EW powder was added into the PCL/PLGA/CHA solution.

Table 1 shows the compositions of the blended polymer solutions prepared in 12 mL syringes with a 0.05 mm needle. The voltage used was 10 kV, with the distance between the syringes and collector being 10 cm, with a flow rate 30–35 μL m^{-1}. The nanofiber membranes were characterized by XRD, DSC, FTIR, SEM, and cell viability tests.

2.4 Sample characteristics

2.4.1 XRD analysis. The crystallographic properties of CHA powder and the PCL/PLGA, PCL/PLGA/CHA, and PLC/PLGA/CHA/EW nanofiber membranes were determined by X-ray diffraction (XRD, PANanalytical Type X'Pert Pro, Japan). The XRD data were recorded at 20°–60° using Cu–K radiation at λ = 0.154 nm.

2.4.2 FTIR analysis. Fourier transform infrared spectroscopy (FTIR, Thermo Nicolet iS10, Japan) was used to determine the functional groups in CHA powder and the nanofiber membranes after immersion in simulated body fluid (SBF) for 3–9 days. The FTIR instrument was operated in the range of 600–4000 cm^{-1}.

2.4.3 SEM morphological analysis. The CHA particles and nanofibers' morphology were observed by scanning electron microscopy (SEM, Joel JSM-6510LA, Japan). The average fiber diameter was calculated based on the measurements of 100

Table 1 The composition of the polymer blends in the study

Materials	Composition of the polymer blends	Sample code
PCL (10%), PLGA (10%) CHA (0.008 g), EW (0.02 g), DMF	PCL (5 mL)	PCL
	PCL : PLGA (4 mL/2 mL)	PCL/PLGA
	PCL : PLGA : CHA (4 mL/2 mL/0.008 g)	PCL/PLGA/CHA
	PCL : PLGA : CHA : EW (4 mL/2 mL/0.008 g/0.02 g)	PCL/PLGA/CHA/EW

randomly selected fibers using ImageJ software. Energy dispersive X-ray spectroscopy (EDS) was used to determine the calcium (Ca) and phosphorus (P) contents of the CHA powders.

2.4.4 DSC analysis. Thermal analysis of the nanofiber membranes was performed to determine the melting point and enthalpy by differential scanning calorimetry[19,20] on a (DSC)-60 Plus Shimadzu binder in a temperature range of −140 °C to 600 °C with a standard cooling chamber and using liquid nitrogen with a flow rate of 10 °C m^{-1}. Sample preparation was carried out in crimped aluminum with a 2–2.3 mg sample weight.

2.4.5 Mechanical properties. The tensile tests were carried out using a universal machine testing (UTM, Zwick DOFB.5 TS, USA) with a 10 mm min^{-1} crosshead speed. The initial sample size was 10 mm × 40 mm, with four samples tested for each type of electrospun fiber.

2.5 Swelling ratio

The swelling characteristics of the electrospun fibers were evaluated for water absorption using the method of Meng *et al.*[21] The fiber was cut into a rectangular shape (10 × 10 mm), weighed (W_o), and then immersed in distilled water for 24 h. Next, the samples were rinsed and placed on filter paper to remove excess water, and then weighed in a wet state (W). The swelling ratio was calculated according to the equation,

$$\text{Swelling ratio } (\%) = \frac{W - W_o}{W_o} \times 100\%$$

2.6 Nanofiber bioactivity in SBF

Bioactivity is essential to a scaffold to form an interface bond between bone and tissue before application. Evaluation of the nanofibers' bioactivity followed the protocol proposed by Kokubo *et al.*[22] First, samples (10 × 10 mm) were immersed in SBF solution for 3 to 9 days, and dried at room temperature, and then, the apatite mineralization on nanofibers composition was reviewed by SEM-EDS.

2.7 Cell viability by MTT assay

2.7.1 NIH-3T3 fibroblast cell culture. Fibroblasts were grown in DMEM high glucose medium (Gibco, CA, USA), supplemented with bovine calf serum 10% (Sigma, MA, USA), Pen Strep 2% (Gibco, CA, USA), and Fungizone 0.5% (Gibco, CA, USA).

2.7.2 Cell harvesting and cell cultivation. Briefly, NIH-3T3 cells ready for harvest were observed under an inverted microscope under 80% confluence. Next, a 24-well plate (SPL, Gyeonggi-do, Korea) was prepared and PCL/PLGA/CHA/EW (10 × 10 mm) sterilized nanofiber membrane was added. Next, 200 μL per well of cell suspension with a cell count of 5×10^4 for each well was added and incubated for 30 min. Finally, 800 μL of complete medium was added in to each well, and then incubated for 48 h treatment.

2.7.3 MTT assay. The medium in each well was removed carefully using a pipette, and an MTT reagent 0.5 mg mL^{-1} (Biobasic, NY, USA) was added to each well (1 mL) and incubated for 4 h. Then, the MTT solution was discarded and DMSO (Merck KGaA, Darmstadt, Germany) was added as 1 mL per well and incubated for 30 min until the crystals dissolved in DMSO. The absorbance of the solution was read using Tecan Spark® (Tecan Trading AG, Switzerland) at a wavelength of 570 nm, and the cell viability was determined using the equation,

$$\text{Cell viability } (\%) = \frac{\text{absorbance of sample} - \text{absorbance of medium control}}{\text{absorbance of control} - \text{absorbance of medium control}} \times 100\%$$

2.8 Antibacterial activity by disk diffusion

2.8.1 Preparation of the medium nutrient broth agar. First, 1.3 g nutrient broth was prepared and then 100 mL of distilled water was added in an Erlenmeyer flask and then 2% agar was added to the total solution (2 g). The solution was heated and stirred until homogeneous. Next, the nanofiber membranes were sterilized by autoclaving and then stored in a Petri dish.

2.8.2 Subculture preparation. The culture medium was inoculated in sterile conditions using the Bunsen burner and incandescent Osse and was allowed to stand for 24 hours. Next, the culture was transferred into sterile distilled water and homogenized with a vortex. 100 microliter culture inoculum was applied onto media in a Petri dish. Using tweezers, the sample was added into the media filled with culture, followed by 10 microlites of positive and negative control. The dish was then tightly closed and sealed. After being incubated for 24 hours, the antibacterial inhibition zone was observed.

3. Results and discussion

3.1 Characteristics of carbonate-hydroxyapatite and nanofiber

The FTIR spectrum of CHA is shown in Fig. 2a, revealing several absorption peaks at 871 cm^{-1} [CO_3^{2-}/carbonate (plane bending) type B], 1417–1465 cm^{-1} [CO_3^{2-}/carbonate (asymmetric stretching) type B], 1024 cm^{-1} [PO_4^{3-}/phosphate (asymmetric stretching)], and 3392 cm^{-1} [presence of OH-hydroxyl (ion stretching)].[23]

SEM imaging of CHA (Fig. 2b) showed a uniform grain size <1 μm, while the EDS results showed the presence of phosphate, calcium, and oxygen elements with high absorption peaks. In addition, the EDS data for CHA (oven-dried) showed the stoichiometry of Ca/P of 1.65.

3.1.1 XRD analysis. The XRD spectrum of CHA (Fig. 3) showed absorption peaks with identical phases (2θ, hkl) at 21.8° (200), 31.7° (211), and 32.9° (300), in accord with JCPDS

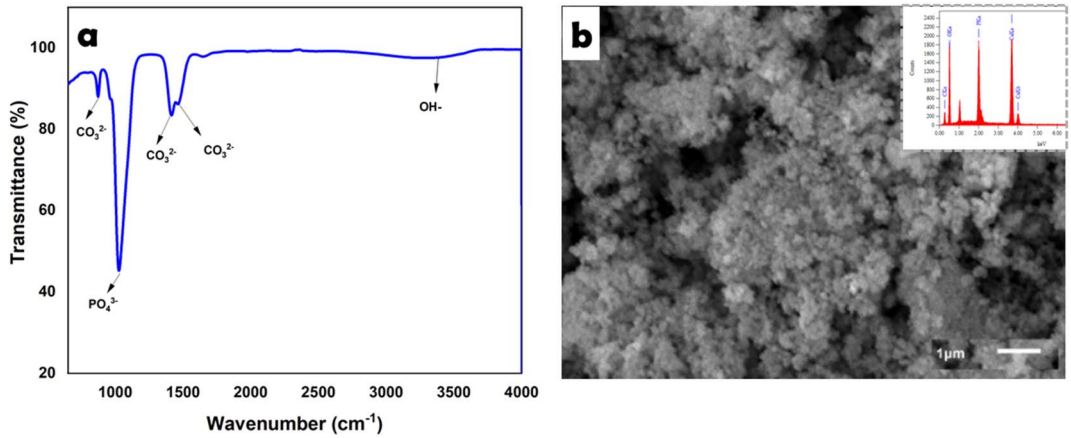

Fig. 2 Characteristic FTIR (a) and SEM-EDS (b) analyses of CHA.

data.[12,23,24] Based on the Debye–Scherrer equation,[25] the estimated crystal size of CHA and the crystallinity were 16.3 nm, and 63%, respectively.

The PCL/PLGA, PCL/PLGA/CHA, and PCL/PLGA/CHA/EE spectra showed the same peaks (2θ) at 21° and 23°, with estimated crystal sizes (according to Scherrer's equation) of 17.7, 12.6, and 13.6 nm, respectively. The phase angles of the nanofibers showed almost the same peaks as pure PCL, at 2θ (hkl) 21.3° (100) and 23.7° (200),[26–28] with sharp peaks. PCL was thus a semi-crystalline polymer, while PLGA and EW were amorphous. The crystallinity of PCL/PLGA, PCL/PLGA/CHA, and PCL/PLGA/CHA/EW were 31%, 32%, and 46% respectively, with high-intensity and sharp peaks. The PCL/PLGA nanofibers had high-intensity peaks at 21.1° and 23.4°, which were shifted to the left (~0.3°), while adding CHA in PCL/PLGA/CHA decreased the intensity.

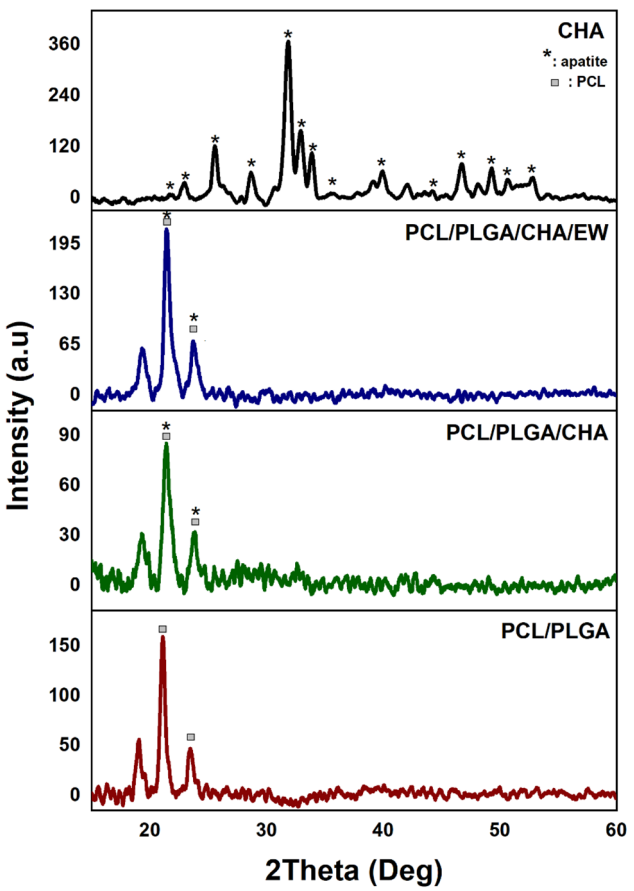

Fig. 3 XRD spectra of CHA and the nanofibers.

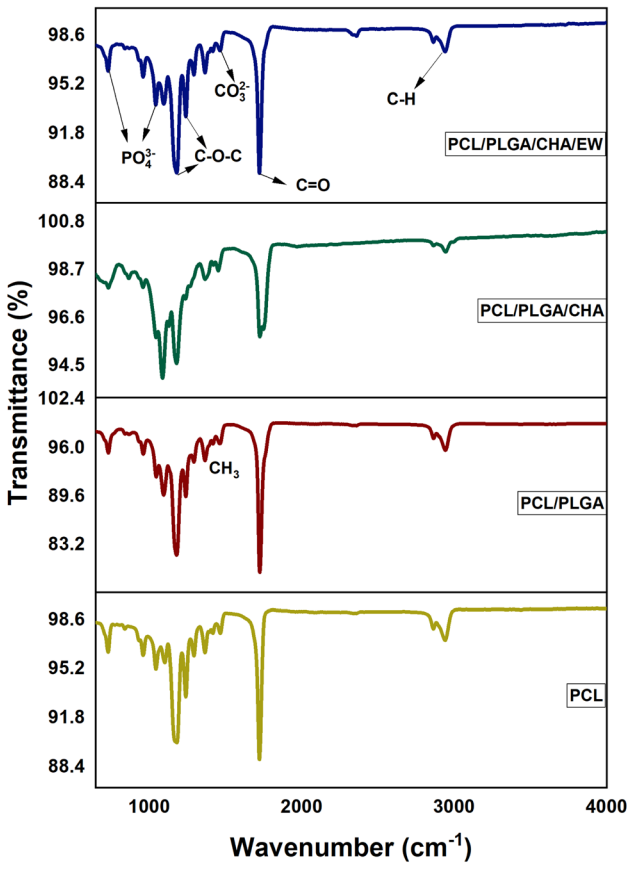

Fig. 4 FTIR nanofibers of PCL, PCL/PLGA, PCL/PLGA/CHA, and PCL/PLGA/CHA/EW.

3.1.2 FTIR. The FTIR spectrum of the nanofibers is shown in Fig. 4 for PCL showing doublet absorption peaks at 2940–2944 (C–H, asymmetric stretching) and 2863 cm^{-1} (C–H, symmetric stretching), and at 1724 cm^{-1} (C=O, stretching),[30] 1240 cm^{-1} (C–O–C, asymmetric stretching), and 1180 cm^{-1} (C–O–C, symmetric stretching).[1,29]

The PCL/PLGA spectra showed absorption peaks nearly the same as for PCL. The pure PLGA spectrum [6] showed peaks at 2996 cm^{-1} (C–H, asymmetric stretching), 1750 cm^{-1} (C=O, stretching), 1455 cm^{-1} (C–H, bending), and at 1080 cm^{-1}, and 1179 cm^{-1} (C–O–C stretching).

The PCL/PLGA spectrum showed typical absorption band characteristics at 2942–2863 cm^{-1}, referring to C–H asymmetric and symmetric stretching, and 1725–1750 cm^{-1}, referring to an ester group (C=O). The peaks at 1239, 1179, and 1094 cm^{-1} were for C–O–C stretching, and the peak at 2942 cm^{-1} was C–H stretching.

The presence of CHA on the PCL/PLGA/CHA nanofibers was indicated by a change in the absorption intensity at 1725 cm^{-1} and the appearance of two sharp peaks at 1180 and 1087 cm^{-1}. The absorption peak at 3596 cm^{-1} referred to the presence of OH-hydroxyl (ion stretching), 2942 cm^{-1} to C–H (asymmetric stretching), 2860 cm^{-1} to C–H (symmetric stretching), and 1725 to C=O (stretching). The peak at 1454 cm^{-1} referred to CO_3^{2-}/carbonate (asymmetric stretching) type B, while other peaks were at 1179 cm^{-1} for C–O–C (stretching), 1089 cm^{-1} for C–O–C (stretching), 1044 for PO_4^{3-}/phosphate (asymmetric stretching), and 865 cm^{-1} for CO_3^{2-}/carbonate (plane bending).

The FTIR spectra of all the samples showed a single peak at 1724 cm^{-1}, which was related to the carbonyl group in the crystalline region. The highest peak intensity was in the PCL/PLGA/CHA sample (95.7%), followed by PCL/PLGA/CHA/EW (89%), PCL (88%), and PCL/PLGA (79.5%). The intensity at this region decreased after SBF immersion treatment for 3–9 days, as shown in Fig. 5.

Fig. 5 shows the FTIR analysis of the nanofibers after being immersed in SBF solution for 3 and 9 days. All the samples showed the same spectral pattern, absorption band, and intensities. Significant absorption bands at 3200–3500 cm^{-1} and 1638–1641 cm^{-1} were identified for the hydroxyl group and the amide/amino acid group. The behavior of the nanofibers after 3 days of SBF immersion showed a transmittance (at 3200–3500 cm^{-1}) of around 60% for PCL, PCL/PLGA, and PCL/PLGA/CHA, and 64% for PCL/PLGA/CHA/EW. At 9 days of SBF immersion, PCL/PLGA, PCL/PLGA/CHA, and PCL/PLGA/CHA/EW were around 64–66%, while PCL was 68%. These results show that all the nanofiber blends with PCL had hydrophobic properties, which meant a longer degradation time. Therefore, the absorption intensity of nanofibers in the SBF immersion affected the nanofiber size as confirmed by SEM morphology.

3.1.3 SEM morphology. The flow rate in the electrospinning process influences the morphology of the nanofibers. The distance between the syringe-collector, the voltage, and the solvent used in the electrospinning process, as shown in Fig. 6, will affect the size of the nanofibers,[31,32] and the mechanical properties of the nanofibers.

Electrospinning produced nanofiber diameters from 100–600 nm to 1000 nm.[33] The increase in fiber diameter was also influenced by adding composites in the PCL polymer. PCL, PCL/PLGA, PCL/PLGA/CHA, and PCL/PLGA/CHA/EW nanofibers had

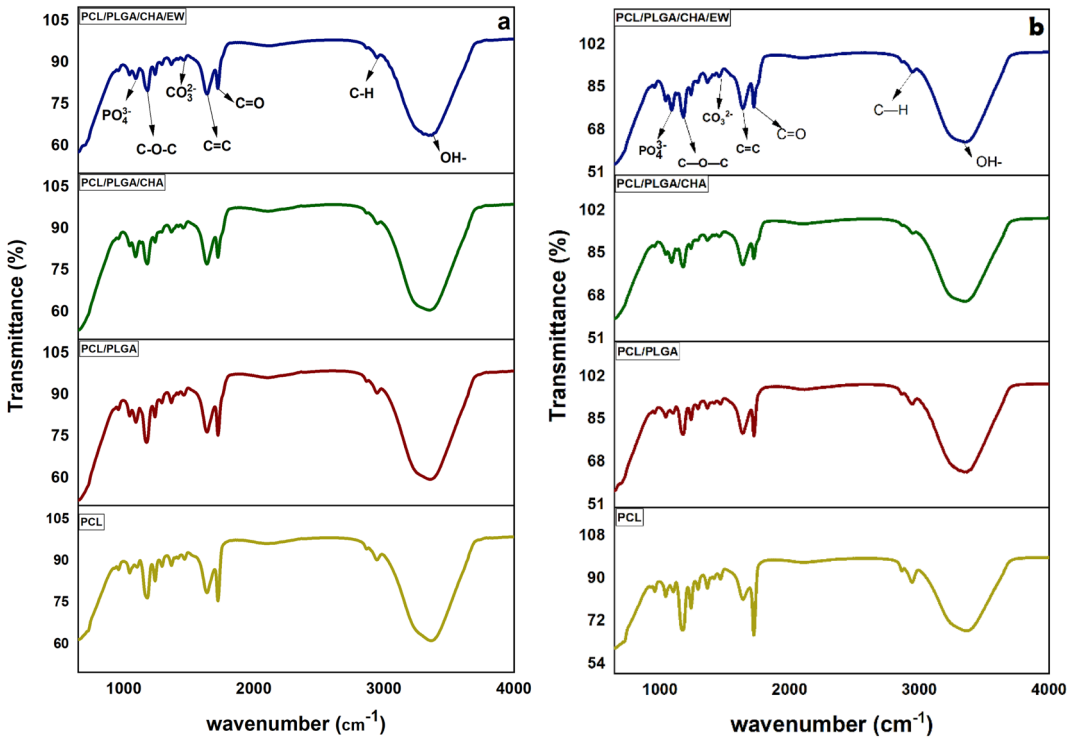

Fig. 5 FTIR spectra of the nanofibers after the SBF immersion for 3 (a) and 9 days (b).

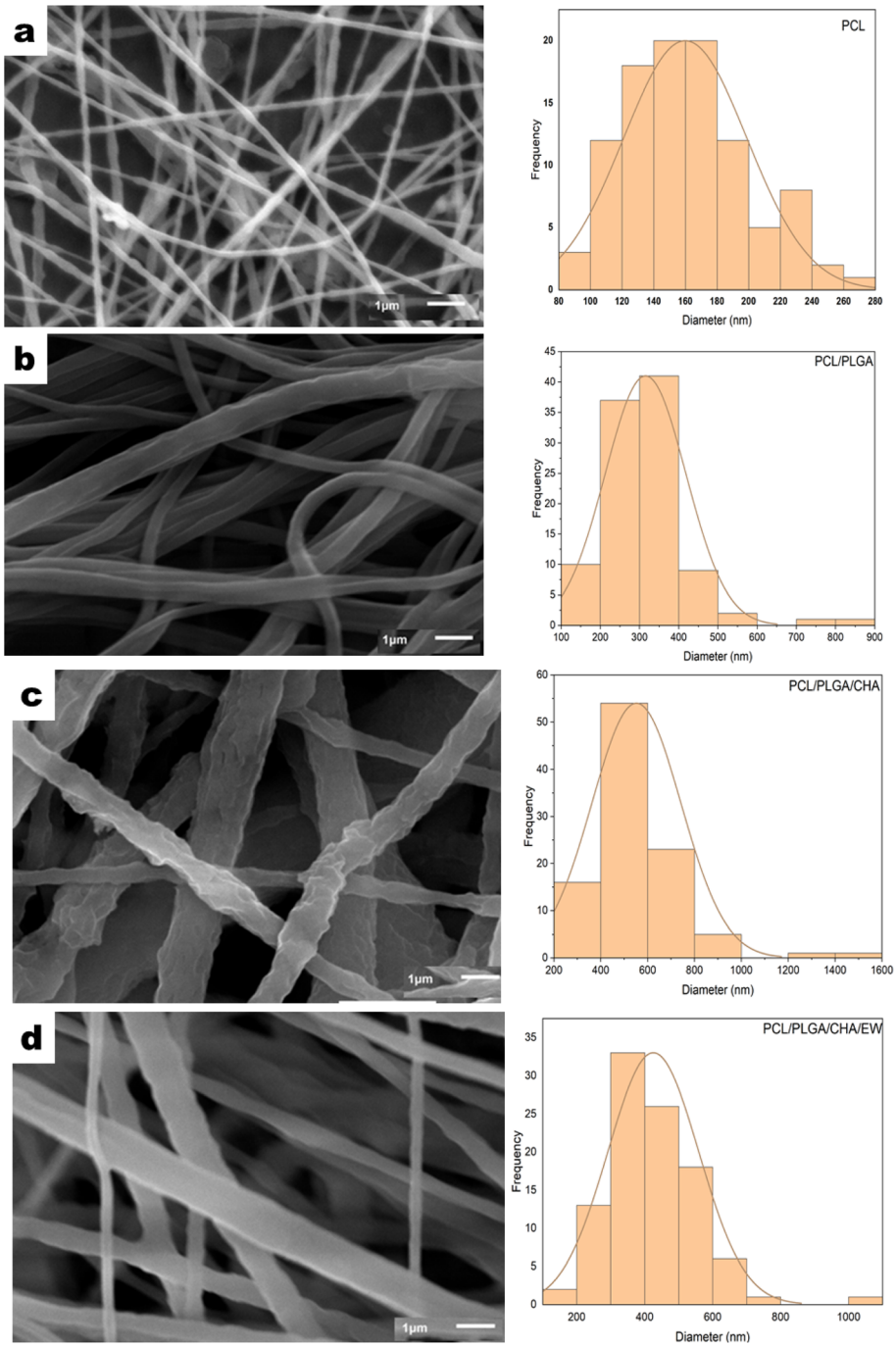

Fig. 6 The SEM morphology and distribution of the diameters of PCL (a), PCL/PLGA (b), PCL/PLGA/CHA (c), and PCL/PLGA/CHA/EW (d) with *×10 000 magnification.

Table 2 The temperature of melting and enthalpy of fusion

	Melting range of PCL (°C)			$\Delta H_{(PCL)}$
Sample	T_{onset}	T_m	T_{endset}	(J g^{-1})
PCL	60	64.45	68.21	23.8
PCL/PLGA	57.87	63.12	66.47	33.54
PCL/PLGA/CHA	59.85	64.67	68.23	16.54
PCL/PLGA/CHA/EW	55.03	60.92	64.91	36.42

fibers with diameters of 152.8 ± 3.5 nm, 304 ± 2.4 nm, 474.68 ± 27.17 nm, and 404.8 ± 10 nm, respectively. The increased fiber diameter was due to various factors, including the solution viscosity, surface tension, applied voltage, and crystallization characteristics of the polymer. Previous research has shown that the solution viscosity had a more significant influence on the average increase in fiber diameter. Increased diameters of the fibers were prepared in the pretreatment of the electrospinning process to enhance the mechanical properties of the fibers.

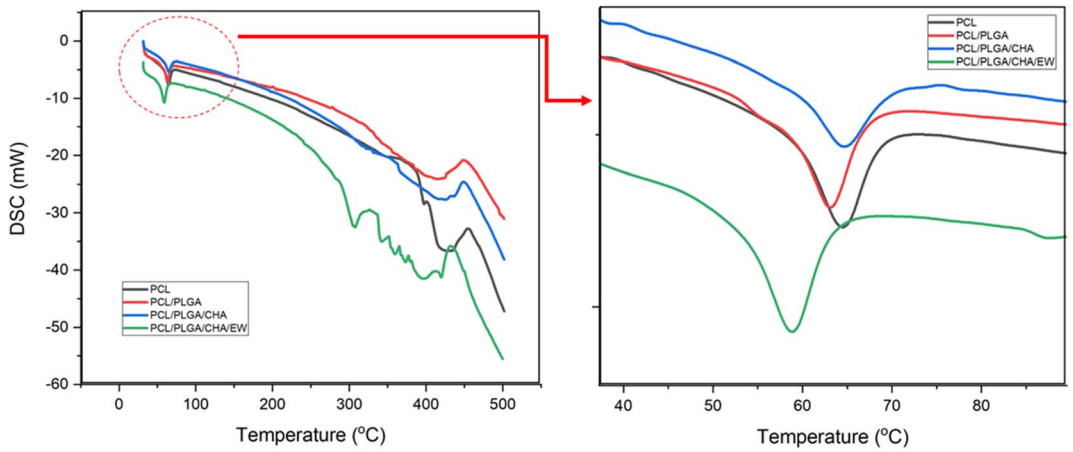

Fig. 7 The DSC curve for PCL, PCL/PLGA, PCL/PLGA/CHA, and PCL/PLGA/CHA/EW.

The morphology of the PCL nanofibers fabricated with a flow rate of 1 mL m^{-1} shows beads on the surface of the nanofibers (Fig. 6a) due to the low conductivity of the PCL, which will produce a small net charge on the droplet surface.[34] Therefore, for meeting application requirements such as in bone grafts, PCL blended nanofibers were fabricated with increasing the flow rate to 30–35 μL m^{-1}.

The addition of PLGA (10%) increased the nanofibers size of PCL/PLGA up to 50%, with the formation of a cylindrical shape, continuous fibers, and a smooth surface (Fig. 6b). The addition of CHA (0.08 g) increased the size of the nanofibers PCL/PLGA/CHA by up to 64%, producing fibers with a rough, continuous cylindrical surface due to the CHA crystals. However, the morphology of the PCL/PLGA/CHA/EW showed cylindrical-continuous nanofibers and porosity, with smaller nanofibers than PCL/PLGA/CHA, due to the protein binding process with CHA through a phosphorylation process, whereby smaller CHA particles could absorb the EW, and change the surface of the nanofiber.

3.1.4 DSC analysis. DSC analysis was used to investigate the thermal properties of the PCL and PCL blended nanofibers, with the results presented in Table 2 and Fig. 7. The DSC curve for PCL showed a melting point of 64.45 °C, while PCL/PLGA showed a melting point of 63 °C, but in the range of 57–66 °C.[35] The melting point of PCL decreased when adding EW in PCL/PLGA/CHA/EW to 60.92 °C, with sharp endothermic peaks observed. PCL/PLGA/CHA/EW had the lowest melting point, which was due to the presence of EW, which showed denaturation of the main protein in egg white, with a gradual denaturation starting at a temperature of 60–62 °C.[36] We presumed that the EW protein binds CHA *via* phosphorylation and caused these samples to have a lower boiling point than PCL due to the amorphous nature of EW protein. Meanwhile, the melting point of PCL/PLGA/CHA was 64.67 °C with a broad endothermic peak, due to CHA substitution, where CHA has a high melting point.

The DSC curve of PCL/PLGA/CHA showed a broader endothermic peak and lower enthalpy of fusion. This is because the melting points of PCL and PLGA were below 65 °C, while CHA had a higher melting point of ~1000 °C. The low enthalpy due to the internal energy of the sample was directly related to temperature. The DSC curves for all samples showed PCL decomposed in the 350–430 °C range, while PCL/PLGA/CHA/EW showed gradual EW decomposition in the 270–400 °C range, as previously reported.[37]

3.1.5 Mechanical properties. The mechanical properties of PCL and the PCL blends were analyzed and the results are summarized in Table 3. The mechanical properties tests of PCL (10%) showed a lower Young's modulus and high tensile strength compared to the blended PCL nanofibers (Fig. 8). However, the PCL/PLGA nanofibers showed an increase in Young's modulus and tensile strength greater than PCL. Furthermore, adding CHA in PCL/PLGA/CHA increased the Young's modulus, with a relative change in tensile strength too, but decreased the elongation of break. Furthermore, the PCL/PLGA/CHA/EW fibers showed reduced stiffness with the decrease in Young's modulus and increase in elongation at break. This phenomenon shows that adding CHA could increase the stiffness of PCL/PLGA/CHA with an increase in Young's modulus and giving a greater tensile strength.

Table 3 The mechanical properties of the nanofibers

Sample	Elongation at break (%)	Young's Modulus (MPa)	Tensile strength (MPa)
PCL	11.25 ± 2.50	85.58 ± 15	9.04 ± 0.87
PCL/PLGA	13.12 ± 1.25	262.74 ± 46	35.21 ± 3.68
PCL/PLGA/CHA	8.08 ± 3.17	412.94 ± 102	33.16 ± 4.21
PCL/PLGA/CHA/EW	20 ± 7.07	172.48 ± 75	29.50 ± 8.64

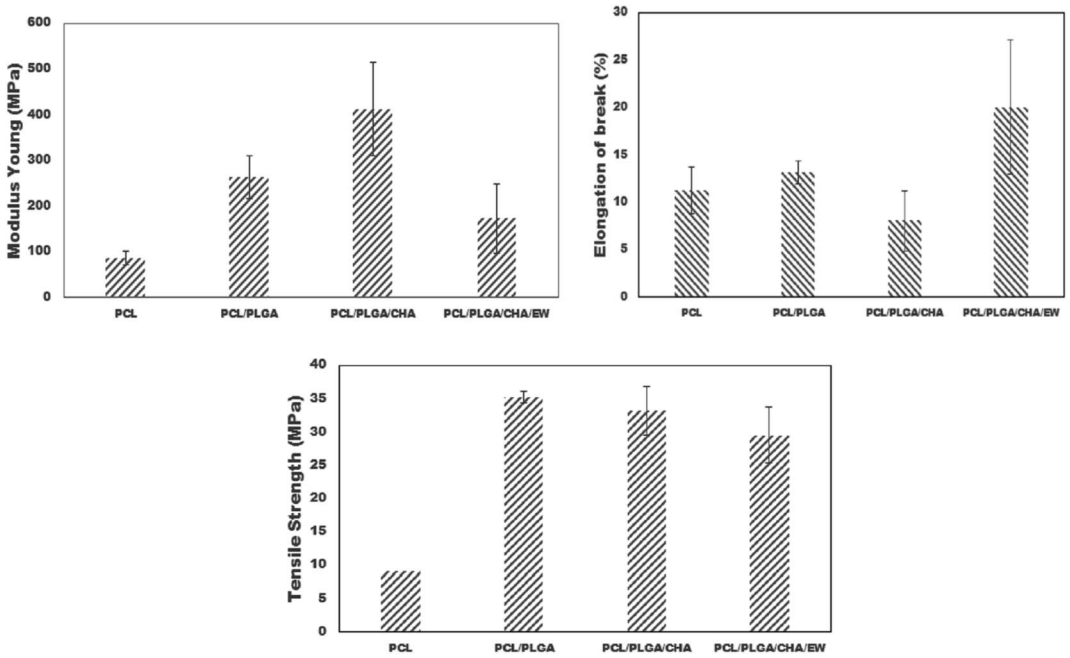

Fig. 8 The Young's modulus, elongation at break, and tensile strength of the nanofibers.

On the contrary, adding EW to PCL/PLGA/CHA/EW significantly decreased the Young's modulus, but increased the elongation at break. The higher Young's modulus of a material will reduce the material's elasticity and *vice versa*. The mechanical properties of PCL/PLGA/CHA/EW showed the highest elongation at break, indicating that the addition of EW can increase the implant ductility when applied and can resist changes in shape without cracks. The tensile strength of nanofibers is highly dependent on the polymer composition and the size distribution of the fibers.

The key fabrication parameters (solution concentration, flow rate, voltage, collector distance) influence the nanofiber properties, whereby a high concentration of the solution will reduce the porosity of the fibers and increase the mechanical characteristics (Young's modulus and tensile strength).[38]

3.2 Swelling ratio

Swelling tests were performed for the blended PCL nanofibers through immersion in distilled water for 24 h at room temperature, as shown in Fig. 9. Quantitative analysis showed significant increases in the swelling ratios (%) of PCL, PCL/PLGA, and PCL/PLGA/CHA nanofibers of 100 ± 0.01, 113.15 ± 3.72, 140 ± 37.71, and 53.78 ± 15.05, respectively. PCL and PLGA are hydrophobic polymers,[39] but the test results showed increased swelling ratios. PCL is a semi-crystalline polymer with only a part of the surface area permeated; but with amorphous PLGA, it can increase the swelling ratio because permeation occurs through mass transport only through the amorphous polymer phase, not at all through the crystal.[41] PCL and PLGA also have the physical adsorption properties of most polymers used in electrospinning.[42] The swelling test process for 24 h showed increases in the swelling ratios of PCL/PLGA, due to the contribution of PLGA being easily degraded through hydrolytic cutting and then being able to absorb water/swell. The increase in the swelling ratio was also contributed to by the morphology or porosity of the fiber due to water becoming trapped in the pores.[40]

PCL/PLGA/CHA had the highest swelling ratio due to CHA having a hydroxyl group (OH–) and the increased water absorption into the nanofibers.[43] Furthermore, PCL/PLGA/CHA/EW showed the lowest swelling ratio, caused by the addition of the EW composition, which included hydrophobic protein.[44] We presume that a phosphorylation process occurred in the EW and CHA to reduce the water absorption in the samples and make them appear more hydrophobic. The low swelling ratio was also caused by the interaction between calcium ions in CHA and protein, facilitating cross-linking and aggregation of the protein chains and causing a high concentration of calcium ions, which could effectively reduce the swelling capacity of the

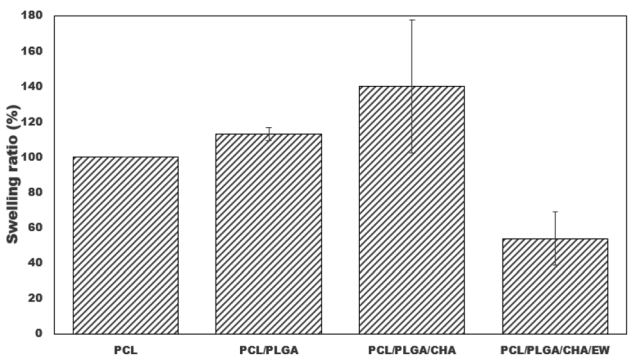

Fig. 9 Swelling ratios of the nanofiber after immersion in distilled water for 24 hours (*: $p < 0.05$).

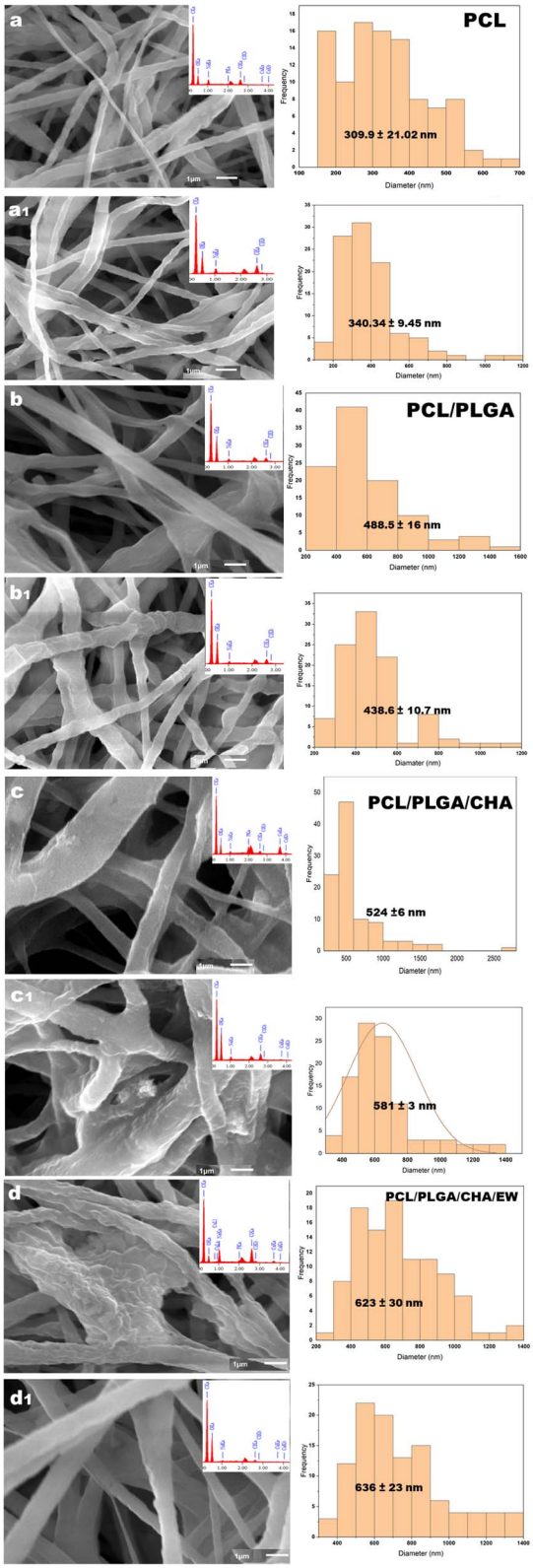

Fig. 10 The SEM morphology and nanofiber diameter after immersion in the SBF for 3 and 9 days for PCL (a and a1), PCL/PLGA (b and b1), PCL/PLGA/CHA (c and c1), and PCL/PLGA/CHA/EW (d and d1).

original egg white. The swelling behavior of PCL/PLGA/CHA/EW showed morphological changes after the immersion process in SBF after 3 to 9 days, as confirmed by the FTIR data and SEM morphology. Swelling behaviors were reported in previous studies, reporting that PCL/EW fibers showed hydrophilic properties according to contact angle (CA) testing, showing a CA of 70° at the beginning, followed by a rapid decrease with the absorbance of water droplets throughout the test time.[37]

3.3 Bioactivity in SBF

Fig. 10 shows the SEM-EDS morphology and nanofiber size distribution after SBF immersion for 3 and 9 days. The nanofibers before and after immersion in SBF showed an increase in the concentration of Ca and P ions after three days,[45] but on day 9, there was a decrease in the concentration of both ions (Ca and P), caused by deposition and melting processes in SBF solution, which was confirmed by previous studies.[46–48] In addition, SEM morphology analysis of the nanofibers showed changes in their surface and diameter size after immersion in SBF.

On the 3rd day of SBF immersion, the fibers showed an increase in diameter, and lumps grew on the fiber surface, which indicated apatite growth, which was typically seen in all the samples. On the 9th day, the fibers showed an increased diameter for PCL, PCL/PLGA/CHA, and PCL/PLGA/CHA/EW, but the PCL/PLGA nanofiber size decreased slightly (Fig. 11), due to the composite compositions (PCL : PLGA, 2 : 1) and even hydrophobicity properties, so the immersion process in SBF after nine days did not affect the fiber size. PCL/PLGA/CHA/EW had the highest fiber diameter after SBF immersion for 9 days, indicating the ability of this nanofiber to absorb a lot of water due to the protein content of EW, which is an important parameter application due to its cell adhesion ability.

3.4 Cell viability assay

Biocompatibility testing of PCL/PLGA/CHA/EW was performed using NIH-3T3 fibroblast cells after 48 h of incubation, as shown in Fig. 12. Fibroblasts are the most common types of native connective tissue cells and have interconnections with cartilage cells and bone cells, are responsible for the

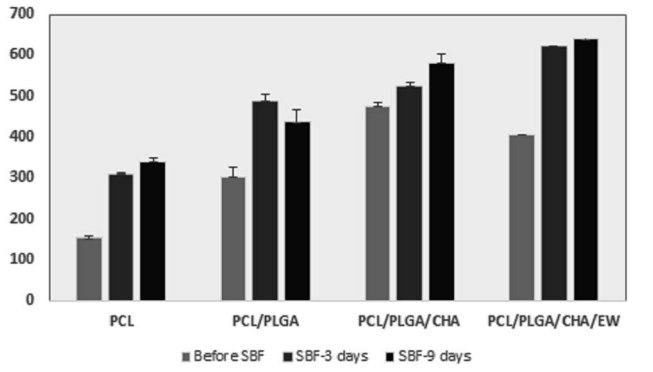

Fig. 11 Diameters of the nanofiber after immersion in the SBF for 3 and 9 days.

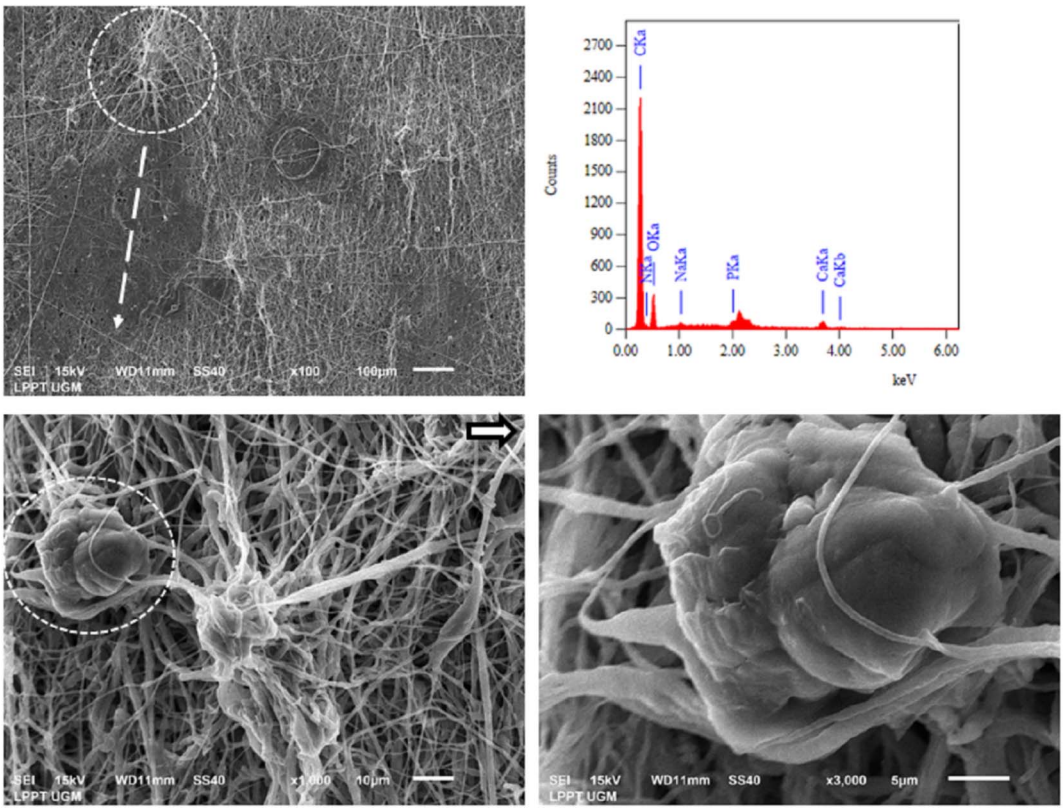

Fig. 12 The SEM morphology of NIH-3T3 fibroblast cells on the surface of PCL/PLGA/CHA/EW.

architectural framework of the body, and can synthesize collagen, elastic fibers, and proteoglycans from the extracellular matrix.[49] Collagen produced by fibroblast cells connects the ends of broken bones (fibrocartilaginous callus), and then osteoblast cells will begin to form new spongy bone tissue. So indirectly, fibroblast cells help regulate bone damage through the osteoclast/osteoblast axis.[50]

Fig. 12 shows the PCL/PLGA/CHA/EW surface with the distribution of fibroblast cells attached (yellow arrow), with a magnification of 1000× (yellow circle). The attachment of fibroblast cells that bind and form the surrounding tissue can be seen with the appearance of fibroblast cells. The EDS spectra showed the presence of elements of calcium and phosphate, which are active minerals that formulate bone around the fibroblast cell tissue. MTT assay of fibroblast cells at 48 hours had a cell viability of 85% against control cells (100%) when used as a hydroxyapatite nanoparticle-based gel (20 wt%) for enamel remineralization, showing its cytocompatibility.[51]

The increase in absorbance after 48 h was due to the high optical density (OD) with the increase in cell concentration, indicating nanofiber biocompatibility; as reported, PCL proliferation with fibroblast cells showed an increase in OD after 48 h.[52] Fibroblast cells participate in bone remodeling by communicating between several types of bone tissue cells. With abundant fibroblasts around osteoblasts, secreting ECM can encourage the regeneration of muscle tissue, nerves, arteries, and bone tissue.[53]

3.5 Antibacterial analysis

Antibacterial activity tests on the PCL-based nanofiber membranes on PCL/PLGA. PCL/PLGA/CHA and PCL/PLGA/CHA/EW were carried out using the disk diffusion method against *E. coli* and *S. aureus* bacteria (Fig. 13). As previously reported, PCL[54] and PLGA[55,56] had no antibacterial activity. The antibacterial agent used in the fabrication of nanofiber membranes was egg white (EW), which has antibacterial properties.[9,11,12,57,58]

The antibacterial activity of PCL/PLGA, PCL/PLGA/CHA, and PCL/PLGA/CHA/EW against *E. coli* showed a clear area in the positive control (chloramphenicol), while the nanofiber swarmed with bacteria without a clear zone around. *Escherichia coli* is a Gram-negative bacterium that is resistant to antibiotics. The antibacterial activity of EW against *E. coli* showed no antibacterial activity, as previously reported by Abdel-Shafi *et al.*,[59] but egg yolk (immunoglobulin, (Ig)Y) could inhibit the growth of *E. coli* bacteria.[60,61] The antibacterial activity in the PCL/PLGA/CHA/EW nanofibers came from the EW protein (lysozyme), a hydrolytic enzyme capable of degrading bacterial cell walls against Gram-positive bacteria, such as *S. aureus*.[62] A clear zone was seen in the control for the antibacterial activity of nanofibers against *S. aureus*, and the PCL/PLGA/CHA/EW nanofibers showed low antibacterial activity. An inhibition zone was found with the distribution of bacteria, presumably due to the low concentration of EW (0.02 g) and due to protein denaturation by the DMF solvent.

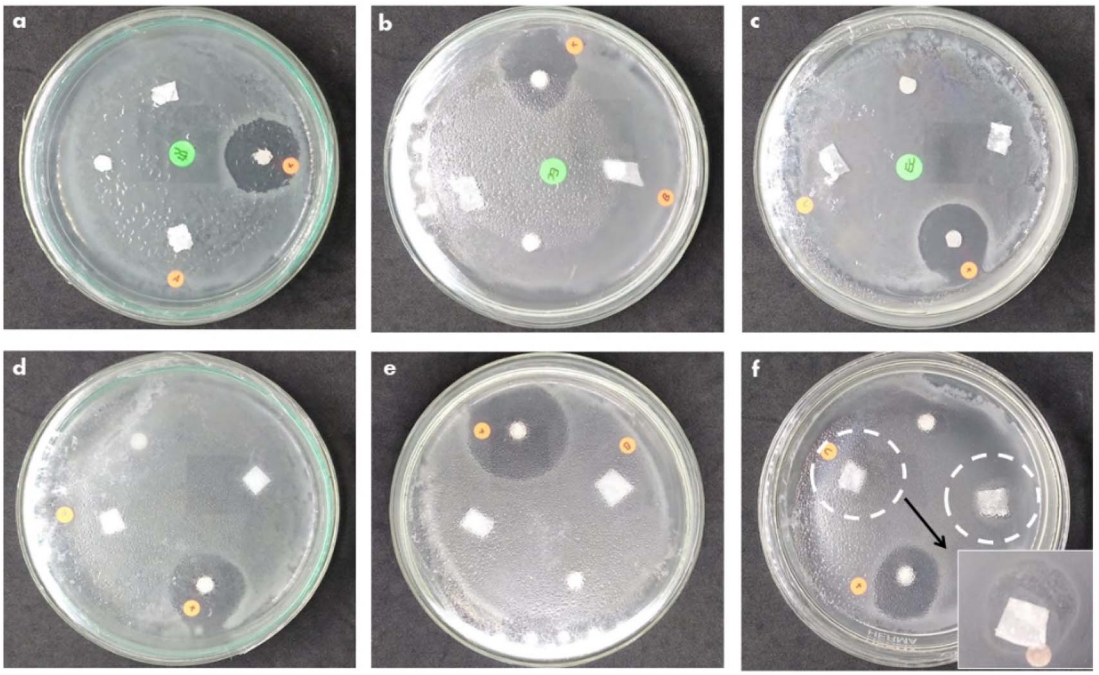

Fig. 13 The antibacterial activity of PCL/PLGA (a and d). PCL/PLGA/CHA (b and e), and PCL/PLGA/CHA/EW (c and f) against *E. coli* (top) and *S. aureus* (bottom).

4. Conclusion

In this research, we successfully fabricated a nanofiber PCL/PLGA doped with CHA and EW by an electrospinning technique that showed unique characteristics. The substitution of CHA and EW greatly influenced the mechanical properties of the nanofiber. The additional CHA (PCL/PLGA/CHA) increased the Young's modulus while EW substitution (PCL/PLGA/CHA/EW) increased the elongation at break. PCL/PLGA/CHA/EW had the highest fiber diameter after SBF immersion for 9 days, indicating the ability to absorb a lot of water, which is an important parameter for its cell adhesion ability. Biocompatibility assay of fibroblast cells on PCL/PLGA/CHA/EW showed good cell proliferation (85%) and the sample with EW with a lower concentration showed ability as an antibacterial agent in PCL/PLGA/CHA/EW against *S. aureus*.

Conflicts of interest

There are no conflicts to declare.

Acknowledgements

The authors would like to thank the Riset Kolaborasi Indonesia (RKI) 2023 Program (2639/UN1/DITLIT/Dit-Lit/PT.01.03/2023) of the Directorate of Research, Universitas Gadjah Mada, Yogyakarta, Indonesia. The authors also express gratitude for the facilities and technical assistance of the Material Physics and Electronics Laboratory and staff of the Integrated Laboratory for Research and Testing (LPPT) Universitas Gadjah Mada, Yogyakarta, Indonesia.

References

1 J. Pawlik, K. Łukowicz, K. Cholewa-Kowalska and A. M. Osyczka, *Mater. Res. Express*, 2019, **6**(8), 1–13.
2 A. Subramanian, U. M. Krishnan and S. Sethuraman, *Ann. Biomed. Eng.*, 2012, **40**, 2098–2110.
3 Y. Qian, H. Chen, Y. Xu, J. Yang, X. Zhou, F. Zhang and N. Gu, *Int. J. Nanomed.*, 2016, **11**, 4157–4171.
4 Z. Wang, R. Liang, X. Jiang, J. Xie, P. Cai, H. Chen, X. Zhan, D. Lei, J. Zhao and L. Zheng, *Mater. Sci. Eng., C*, 2019, **104**, 109796.
5 T. Eren Boncu, A. Uskudar Guclu, M. F. Catma, A. Savaser, A. Gokce and N. Ozdemir, *Int. J. Pharm.*, 2020, **573**, 118758.
6 M. Milosevic, D. B. Stojanovic, V. Simic, M. Grkovic, M. Bjelovic, P. S. Uskokovic and M. Kojic, *Sci. Rep.*, 2020, **10**(1), 11126.
7 N. T. Hiep and B. T. Lee, *J. Mater. Sci.: Mater. Med.*, 2010, **21**(6), 1969–1978.
8 Z. Guo, T. Zhang, K. Fang, P. Liu, M. Li and N. Gu, *Colloids Surf., A*, 2016, **504**, 43–52.
9 N. Guyot, S. Jan, S. Réhault-godbert, Y. Nys, M. Gautier, N. Guyot, S. Jan, S. Réhault-godbert, Y. Nys and M. Gautier, *World's Poult. Sci. J.*, 2013, **69**, 1–15.
10 H. B. Han, X. Li, K. Yu, W. Z. Ma and Z. C. Cao, *Asian J. Anim. Vet. Adv.*, 2011, **6**(7), 667–677.
11 D. J. Patty, A. D. Nugraheni, I. D. Ana and Y. Yusuf, *J. Biomed. Mater. Res., Part B*, 2022, **110**(6), 1412–1424.
12 D. J. Patty, A. D. Nugraheni, I. D. Ana and Y. Yusuf, *J. Biomater. Sci. Polym. Ed.*, 2022, 1–19.
13 M. Alizadeh-Osgouei, Y. Li and C. Wen, *Bioact. Mater.*, 2019, **4**, 22–36.

14 M. Sari, P. Hening, Chotimah, I. D. Ana and Y. Yusuf, *Mater. Today Commun.*, 2021, **26**, 102135.
15 R. M. Anggraini and Y. Yusuf, *IOP Conf. Ser.: Mater. Sci. Eng.*, 2019, **546**(4), 042002.
16 B. ben Nissan, A. H. Choi, and D. W. Green, *Marine-Derived Biomaterials for Tissue Engineering Applications*, Springer Singapore, Sydney, 2019.
17 E. Landi, G. Celotti, G. Logroscino and A. Tampieri, *J. Eur. Ceram. Soc.*, 2003, **23**, 2931–2937.
18 C. Cha, F. Piraino and A. Khademhosseini, *Microfabrication Technology in Tissue Engineering*, Elsevier Inc., 2nd edn., 2014.
19 S. F. Abdellah Ali, *IOP Conf. Ser.: Mater. Sci. Eng.*, 2016, **137**, 012035.
20 M. Avella, M. E. Errico, P. Laurienzo, E. Martuscelli, M. Raimo and R. Rimedio, *Polym. Commun.*, 2000, **41**, 3875–3881.
21 Z. X. Meng, Y. S. Wang, C. Ma, W. Zheng, L. Li and Y. F. Zheng, *Mater. Sci. Eng., C*, 2010, **30**, 1204–1210.
22 T. Kokubo and H. Takadama, *Biomaterials*, 2006, **27**, 2907–2915.
23 M. Fleet, *Carbonated hydroxyapatite: Materials, synthesis, and applications*, 2014.
24 M. Markovic, B. O. Fowler and M. S. Tung, *J. Res. Natl. Inst. Stand. Technol.*, 2004, **109**, 553–568.
25 Z. Hajizadeh, R. Taheri-Ledari, and F. R. Asl, *Heterogeneous Micro and Nanoscale Composites for the Catalysis of Organic Reactions*, Elsevier, 2022, pp. 33–51.
26 X. Wang, H. Zhao, L. S. Turng and Q. Li, *Ind. Eng. Chem. Res.*, 2013, **52**, 4939–4949.
27 S. M. Kamath, K. Sridhar, D. Jaison, V. Gopinath, B. K. M. Ibrahim, N. Gupta, A. Sundaram, P. Sivaperumal, S. Padmapriya and S. S. Patil, *Sci. Rep.*, 2020, **10**(1), 18179.
28 S. Gautam, A. K. Dinda and N. C. Mishra, *Mater. Sci. Eng. C*, 2013, **33**, 1228–1235.
29 J. E. Oliveira, L. H. C. Mattoso, W. J. Orts and E. S. Medeiros, *Adv. Mater. Sci. Eng.*, 2013, **2013**, 1–14.
30 O. Gil-Castell, J. D. Badia, I. Ontoria-Oviedo, D. Castellano, P. Sepúlveda and A. Ribes-Greus, *Mater. Sci. Eng., C*, 2020, **107**, 1–14.
31 T. J. Sill and H. A. von Recum, *Biomaterials*, 2008, **29**, 1989–2006.
32 A. Ghajarieh, S. Habibi and A. Talebian, *Russ. J. Appl. Chem.*, 2021, **94**, 847–872.
33 M. Milosevic, D. Stojanovic, V. Simic, B. Milicevic, A. Radisavljevic, P. Uskokovic and M. Kojic, *Materials*, 2018, **11**(12), 2416.
34 W. Zeng, N. Cheng, X. Liang, H. Hu, F. Luo, J. Jin and Y. Li, *Sci. Rep.*, 2022, **12**, 10900.
35 M. Kemme and R. Heinzel-Wieland, *J. Funct. Biomater.*, 2018, **9**(1), 1–11.
36 T. A. Vilgis, *Rep. Prog. Phys.*, 2015, **78**(12), 124602.
37 N. Z. Renkler, E. Ergene, S. Gokyer, M. Tuzlakoglu Ozturk, P. Yilgor Huri and K. Tuzlakoglu, *J. Mater. Sci.: Mater. Med.*, 2021, **32**(4), 1–11.
38 R. Vasita and D. S. Katti, *Int. J. Nanomed.*, 2006, **1**, 15–30.
39 D. S. Kohane and R. Langer, *Polymeric Biomaterials in Tissue Engineering*, 2008.
40 S. Goreninskii, N. Danilenko, E. Bolbasov, A. Evtina, M. Buldakov, N. Cherdyntseva, M. Saqib, N. Beshchasna, J. Opitz, V. Filimonov and S. Tverdokhlebov, *J. Appl. Polym. Sci.*, 2021, **138**(23), 1–11.
41 J. G. A. Bitter, *Desalination*, 1984, **51**, 19–35.
42 B. Niemczyk-Soczynska, A. Gradys and P. Sajkiewicz, *Polymers*, 2020, **12**, 1–20.
43 I. K. Januariyasa, I. D. Ana and Y. Yusuf, *Mater. Sci. Eng., C*, 2020, **107**, 110347.
44 E. E. G. Rojas, J. S. dos Reis Coimbra, L. A. Minim, S. H. Saraiva and C. A. S. da Silva, *J. Chromatogr. B*, 2006, **840**, 85–93.
45 J. A. Rincón-López, J. A. Hermann-Muñoz, A. L. Giraldo-Betancur, A. de Vizcaya-Ruiz, J. M. Alvarado-Orozco and J. Muñoz-Saldaña, *Materials*, 2018, **11**, 17.
46 C. R. Campion, S. L. Ball, D. L. Clarke and K. A. Hing, *J. Mater. Sci.: Mater. Med.*, 2013, **24**, 597–610.
47 N. Hashim, S. Sabudin, S. Ibrahim, N. M. Zin, S. H. A. Bakar and F. Fazan, *Med. J. Malaysia*, 2004, **59**(Suppl B), 103–104.
48 P. Ducheyne, *Comprehensive Biomaterial*, 2011.
49 B. Alberts, A. Johnson, J. Lewis, M. Raff, K. Roberts and P. Walter, Molecular Biology of the Cell, *Fibroblasts and Their Transformations: The Connective-Tissue Cell Family*, Garland Science, New York, 4th edn, 2002.
50 J. D. Turner, A. J. Naylor, C. Buckley, A. Filer and P. P. Tak, *Advances in Experimental Medicine and Biology*, Springer New York LLC, 2018, vol. 1060, pp. 37–54.
51 M. Sari, D. M. Ramadhanti, R. Amalina, Chotimah, I. D. Ana and Y. Yusuf, *Dent. Mater. J.*, 2022, **41**, 68–77.
52 A. Satish and P. S. Korrapati, *RSC Adv.*, 2015, **5**, 83773–83780.
53 M. Li, A. Zhang, J. Li, J. Zhou, Y. Zheng, C. Zhang, D. Xia, H. Mao and J. Zhao, *Bioact. Mater.*, 2020, **5**, 938–948.
54 X. H. Bai, J. Zhang, G. T. Cheng, X. F. Liu, T. C. Sun, J. Yang, Z. K. Cao, S. Ramakrishna and Y. Z. Long, *J. Mater. Sci.*, 2022, **57**, 3678–3687.
55 F. N. Almajhdi, H. Fouad, K. A. Khalil, H. M. Awad, S. H. S. Mohamed, T. Elsarnagawy, A. M. Albarrag, F. F. Al-Jassir and H. S. Abdo, *J. Mater. Sci.: Mater. Med.*, 2014, **25**, 1045–1053.
56 A. Haider, S. Kwak, K. C. Gupta and I. K. Kang, *J. Nanomater.*, 2015, **2015**, 1–10.
57 K. Thiyagarajan, V. K. Bharti, S. Tyagi, P. K. Tyagi, A. Ahuja, K. Kumar, T. Raj and B. Kumar, *RSC Adv.*, 2018, **8**, 23213–23229.
58 O. Wellman-Labadie, J. Picman and M. T. Hincke, *Br. Poult. Sci.*, 2008, **49**, 125–132.
59 S. Abdel-Shafi, A. Osman, G. Enan, M. El-Nemer and M. Sitohy, *SpringerPlus*, 2016, **5**(1), 1–13.
60 J. Kovacs-Nolan, M. Phillips and Y. Mine, *J. Agric. Food Chem.*, 2005, **53**, 8421–8431.
61 Y. H. Zhen, L. J. Jin, J. Guo, X. Y. Li, Y. N. Lu, J. Chen and Y. P. Xu, *Vet. Microbiol.*, 2008, **130**, 126–133.
62 X. Shi, X. Li, X. Li, Z. He, X. Chen, J. Song, L. Zeng, Q. Liang, J. Li, G. Xu and J. Zheng, *Foods*, 2022, **11**(4), 1–14.